Combined THEMIS and ground-based observations of a pair of substorm-associated electron precipitation events

Mark A. Clilverd,[1] Craig J. Rodger,[2] I. Jonathan Rae,[3] James B. Brundell,[2] Neil R. Thomson,[2] Neil Cobbett,[1] Pekka T. Verronen,[4] and Frederick W. Menk[5]

Received 13 June 2011; revised 26 October 2011; accepted 12 December 2011; published 22 February 2012.

[1] Using ground-based subionospheric radio wave propagation data from two very low frequency (VLF) receiver sites, riometer absorption data, and THEMIS satellite observations, we examine in detail energetic electron precipitation (EEP) characteristics associated with two substorm precipitation events that occurred on 28 May 2010. In an advance on the analysis undertaken by Clilverd et al. (2008), we use phase observations of VLF radio wave signals to describe substorm-driven EEP characteristics more accurately than before. Using a >30 keV electron precipitation flux of 5.6×10^7 el. cm^{-2} sr^{-1} s^{-1} and a spectral gradient consistent with that observed by THEMIS, it was possible to accurately reproduce the peak observed riometer absorption at Macquarie Island ($L = 5.4$) and the associated NWC radio wave phase change observed at Casey, Antarctica, during the second, larger substorm. The flux levels were near to 80% of the peak fluxes observed in a similar substorm as studied by Clilverd et al. (2008). During the initial stages of the second substorm, a latitude region of $5 < L < 9$ was affected by electron precipitation. Both substorms showed expansion of the precipitation region to $4 < L < 12$ more than 30 min after the injection. While both substorms occurred at similar local times, with electron precipitation injections into approximately the same geographical region, the second expanded in an eastward longitude more slowly, suggesting the involvement of lower-energy electron precipitation. Each substorm region expanded westward at a rate slower than that exhibited eastward. This study shows that it is possible to successfully combine these multi-instrument observations to investigate the characteristics of substorms.

Citation: Clilverd, M. A., C. J. Rodger, I. J. Rae, J. B. Brundell, N. R. Thomson, N. Cobbett, P. T. Verronen, and F. W. Menk (2012), Combined THEMIS and ground-based observations of a pair of substorm-associated electron precipitation events, *J. Geophys. Res.*, *117*, A02313, doi:10.1029/2011JA016933.

1. Introduction

[2] Understanding the morphology of energetic electron precipitation (EEP) into the atmosphere is an important requirement, both in determining the role of electron losses from the magnetosphere [*Spanswick et al.*, 2007; *Clilverd et al.*, 2008; *Reeves et al.*, 2009] and the subsequent impact of EEP on the atmosphere [e.g., *Seppälä et al.*, 2007, 2009]. Much is already known about the time scales of EEP, with precipitation events occurring over seconds [*Lorentzen et al.*, 2001; *Rodger et al.*, 2007b], minutes [*Millan et al.*, 2002; *Rodger et al.*, 2008], hours [*Kavanagh et al.*, 2007; *Spanswick et al.*, 2007; *Clilverd et al.*, 2008], and days [*Rodger et al.*, 2007c; *Clilverd et al.*, 2010]. What is less well known about these events is the precipitation flux and energy spectrum involved. Detailed knowledge of these parameters would allow more accurate analysis of the role of EEP on magnetospheric loss processes and also of the way EEP couples into the atmosphere.

[3] Accurate measurements of EEP are difficult to make from spacecraft at high altitudes because the bounce loss cone is small at these locations and thus hard to resolve, while at low altitudes the detectors either measure only a fraction of the bounce loss cone or include some of the drift loss cone and occasionally some of the trapped component of the radiation belts [*Rodger et al.*, 2010a]. Some current spacecraft measure only a fraction of the bounce loss cone, with poor energy resolution but reasonable spatial coverage (e.g., SAMPEX and POES). Some have poor energy resolution and do not resolve the bounce loss cone but do have constant limited spatial coverage (e.g., GOES and LANL satellites). Others do not resolve the bounce loss cone but do have reasonable spatial coverage and good energy resolution (e.g., DEMETER and THEMIS).

[1]British Antarctic Survey, Cambridge, UK.
[2]Department of Physics, University of Otago, Dunedin, New Zealand.
[3]Department of Physics, University of Alberta, Edmonton, Canada.
[4]Finnish Meteorological Institute, Helsinki, Finland.
[5]University of Newcastle, Callaghan, Australia.

0148-0227/12/2011JA016933

[4] Ground-based measurements of EEP characteristics rely on monitoring the changes in *D* region ionization caused by the precipitation. Techniques effectively use the ionosphere as a large particle detector [*Clilverd et al.*, 2009], but they suffer from significant limitations as a result of the combination of both EEP energy spectra and precipitation flux, which are important factors in determining the production of the *D* region ionization. Only by using multiparameter and multi-instrument observations of the ionization changes produced by EEP is it possible to accurately characterize the EEP events. The combination of ground-based and satellite measurements provides the clearest morphology of EEP characteristics, and this work builds on previous studies of this kind [e.g., *Clilverd et al.*, 2008, 2010].

[5] Substorms generate EEP through the conversion of solar wind energy stored in the Earth's magnetotail into particle heating and kinetic energy [*Akasofu*, 1964; *Axford*, 1999; *Liu et al.*, 2009a]. The reconfiguration of the magnetosphere generates earthward and tailward flows centered on a reconnection site at ~20–30 R_E in the magnetotail [*Nagai et al.*, 1998; *Liu et al.*, 2009a]. *Liu et al.* [2009b] successfully modeled an observed substorm injection of energetic particles propagating radially inward toward geosynchronous orbit. The model consisted of an earthward dipolarization-like pulse from the magnetotail located beyond 20 R_E, and reproduced most features of the injected particles, including the timing of the injection as observed by different satellites. *Liu et al.* [2009b] observed magnetic field dipolarization signatures at ~−11 R_E to occur ~90 s after tail reconnection signatures at ~−20 R_E. *Spanswick et al.* [2009] studied a substorm on 27 August 2001 in detail, concluding that the magnetic field pulse took ~8 min to propagate from −18 to −6.6 R_E. *Spanswick et al.* [2009] also reported that EEPs were observed on the ground near L = 6.6 and expanded both poleward and equatorward, consistent with the earlier riometer-based survey of *Berkey et al.* [1974].

[6] Typically, EEP from a substorm injection occurs near midnight magnetic local time (MLT), with the precipitation region (in the ionosphere) rapidly expanding eastward with velocities that correspond to electron drift velocities associated with energies of 50–300 keV [*Berkey et al.*, 1974]. The electron energies involved in substorm injections seen by satellites such as LANL are typically 50–1000 keV, with the highest fluxes occurring at the lowest energies [*Baker et al.*, 1985; *Clilverd et al.*, 2008]. While the satellite observations provide some information on the energy spectra of the injected electrons and the fluxes in drift orbit, it is very difficult to determine what proportion of the electrons are being precipitated into the atmosphere through onboard satellite measurements. The primary difficulty is in making observations of electron populations in the spatially narrow loss cone in the magnetosphere, particularly around the geomagnetic equator where geostationary satellites reside.

[7] Energetic electron precipitation during substorms has been studied using riometers [e.g., *Jelly and Brice*, 1967], forward scatter radar [e.g., *Bailey*, 1968], and very low frequency (VLF) radio waves [e.g., *Thorne and Larsen*, 1976]. Riometers observe an absorption maximum that is located close to 65° geomagnetic latitude ($L \sim 6$) but which expands poleward and equatorward within 15 min to cover a latitude range of 60°–73° geomagnetic (L = 4–12). This latitude range is consistent with the observations from particle detectors on DMSP flights [*Sandholt et al.*, 2002]. The VLF radio wave technique is most sensitive to ionization caused by high energy and relativistic electron precipitation energies, typically >100 keV, as these energies ionize the neutral atmosphere in the Earth-ionosphere waveguide i.e., at altitudes below ~70 km [*Barr et al.*, 2000]. The energy spectrum of substorm-driven electron precipitation into the atmosphere was determined using high-altitude balloon measurements of X-ray fluxes and was been found to be of the same form as that of the trapped fluxes [*Rosenberg et al.*, 1972].

[8] In a previous study *Clilverd et al.* [2008] used amplitude-only VLF subionospheric radio wave data from a high-latitude location (L = 999, Casey, Australian Antarctic Division) and electron fluxes from the geostationary satellite LANL-97A, all in the region south of Australia and New Zealand, to describe and model electron precipitation driven by substorm injection events. The energy spectrum observed by the LANL-97A instrument during substorms was used to accurately model the subionospheric radio wave substorm signature seen on the VLF transmitter (NWC, Australia) received at Casey, as well as the substorm-driven riometer absorption levels seen at Macquarie Island (L = 5.4, Australian Antarctic Division). The maximum precipitation rate into the atmosphere was found to be 50%–90% of the peak fluxes measured by the LANL-97A spacecraft.

[9] The enhanced ionization caused by EEP can produce odd nitrogen (NO_x) and odd hydrogen (HO_x) species in the upper and middle atmospheres [*Brasseur and Solomon*, 2005]. HO_x is short-lived but responsible for the catalytic ozone loss at mesospheric altitudes [*Verronen et al.*, 2011], while NO_x is much longer lasting in the absence of sunlight and can be transported to lower altitudes where it can catalytically destroy ozone in the stratosphere, particularly at the poles [*Randall et al.*, 2005; *Seppälä et al.*, 2009]. The altitude and concentrations of NO_x and HO_x produced by EEP are functions of the precipitating electron energy spectrum and flux levels that occur during the precipitation events. Precipitation processes generate a wide range of energy spectra and flux levels, all contributing to the altitude profiles of NO_x and HO_x concentrations at any given time. Radiation belt processes during enhanced geomagnetic activity have been shown to generate EEP in large enough amounts to cause observable chemical changes in the upper atmosphere [*Verronen et al.*, 2011]. Radiation belt processes can generate EEP for long periods (~10 days), which also contributes to their chemical effect in the atmosphere [*Rodger et al.*, 2010b; *Clilverd et al.*, 2010]. In contrast, substorm-driven EEP is short-lived, but can generate EEP with higher fluxes at <500 keV than some radiation belt processes [*Clilverd et al.*, 2008]. As such, it is important that the characteristics of substorm-driven EEPs are understood in detail.

[10] In this study we examine the electron precipitation characteristics from two substorm injection events on 28 May 2010, observed in ground-based data and from the THEMIS E satellite. In an advance on the analysis of substorm EEP effects undertaken by *Clilverd et al.* [2008], which used similar techniques and data sets, here we use phase observations of VLF radio wave signals, in addition to two receiver sites instead of one, and investigate the time evolution of the substorm EEP instead of restricting ourselves to only the peak fluxes. Highly variable winter-nighttime

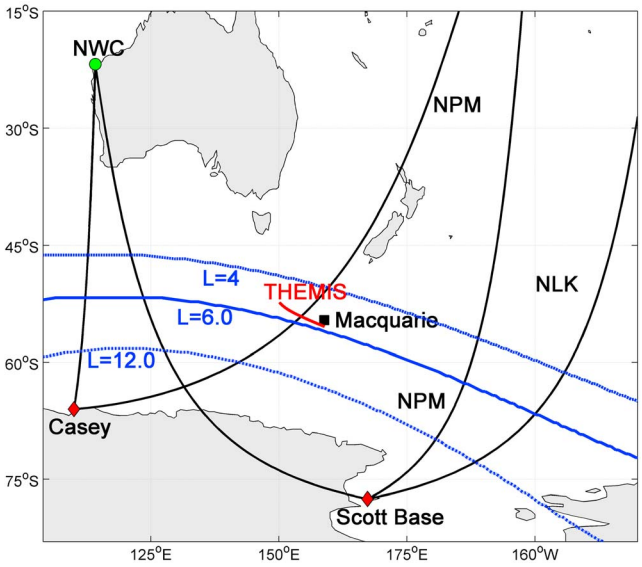

Figure 1. A map of the subionospheric VLF propagation paths from the NWC (green circle), NPM, and NLK transmitters to the Casey and Scott Base receivers in Antarctica (red diamonds). Contours of constant L shells are shown for L = 4, 6, and 12 (blue lines). The locations of the Southern Hemisphere footprint of THEMIS E during the substorm events studied in this paper (red line), and Macquarie Island (solid square) are also indicated.

amplitude values make it difficult to accurately determine the undisturbed behavior and therefore accurately determine any substorm effect using amplitude alone. However, during the nighttime, phase values are relatively steady in undisturbed conditions, and as such we concentrate on the analysis of phase measurements for this study. Also, we expect near-linear phase responses to EEP flux variations rather than the more complex patterns of amplitude behavior as identified by *Clilverd et al.* [2008, Figure 5]. As a result of using phase measurements instead of amplitude, we are able to describe substorm-driven EEPs more accurately than before.

2. Experimental Setup

[11] This study builds on previous work [*Clilverd et al.*, 2008] using very low frequency radio wave observations. Receiver sites are part of the Antarctic-Arctic Radiation-belt Dynamic Deposition VLF Atmospheric Research Konsortia (AARDDVARK) [*Clilverd et al.*, 2009]. Each receiver is capable of receiving multiple narrowband transmissions from powerful man-made communication transmitters. The AARDDVARK network uses narrowband subionospheric VLF/LF data spanning 10–40 kHz to observe changes in the D region ionization levels. This study makes use of the transmissions from NWC (19.8 kHz, 21.8°S, 114.1°E, L = 1.44), NPM (21.4 kHz, 21.4°N, 158.1°W, L = 1.17), and NLK (24.8 kHz, 48.2°N, 121.9°W, L = 2.92) received at Casey, Antarctica (66.3°S, 110.5°E, L > 999), and Scott Base, Antarctica (77.8°S, 166.8°E, L > 32). The transmitter-to-receiver subionospheric great circle paths (GCPs) are shown in Figure 1 as solid lines. Also plotted are the L shell contours for L = 4, 6, and 12. The effects of changing propagation conditions in the mesosphere, which are often due to energetic particle precipitation, can be seen as either an increase or decrease in signal amplitude and typically an increase in phase, depending on the modal mixture of each signal observed [*Barr et al.*, 2000].

[12] The location of the Southern Hemisphere footprint of the THEMIS E satellite from about 11:30–13:30 UT on 28 May 2010 is also shown in Figure 1. The magnetic field model used the International Geomagnetic Reference Field (IGRF) for the internal component, with the Tsyganenko 89 C external field, and K_p set to 3. The location is plotted because we analyze the data from THEMIS E later in this paper, as part of a case study. THEMIS E is part of a multispacecraft mission to study substorms. THEMIS consists of five identical satellites equipped with particle and field instrumentation, including the Solid State Telescope (SST). The SST instrument on THEMIS measures energetic electron populations in the energy range 25–900 keV, providing observations centered on several channels, i.e., 30, 41, 53, 67, 95, 143, 207, 297, 422, and 655 keV [*Angelopoulos*, 2008]. We note here that the THEMIS SST uses an attenuator when passing through the radiation belts in order to protect the instrument. The data presented in this study have the attenuator in operation, and thus the intercalibration of energetic electron energy fluxes from the individual energy channels is uncertain at this time (Angelopoulos, personal communication, 2011).

[13] The riometer data used in this study are provided from Macquarie Island (54.5°S, 158.9°E, L = 5.4). The riometer is a wide-beam, 30 MHz, vertical-pointing parallel dipole system with a time resolution of 1 min. Riometers [*Little and Leinbach*, 1959] observe the integrated absorption of cosmic radio noise through the ionosphere, with increased absorption that is due to additional ionization, for example, due to both proton and electron precipitation. The dominant altitude of the absorption is typically in the range 70–100 km, i.e., biased toward relatively soft particle energies (~30 keV electrons). The colocation of the Macquarie Island riometer in L shell and longitude with the THEMIS E Southern Hemisphere magnetic field line footprint in Figure 1 should be noted.

3. Results

[14] Previous published results from the AARDDVARK system at Casey presented only amplitude measurements from NWC [*Clilverd et al.*, 2008]. Following an upgrade in February 2009 and the December 2008 installation of an additional system at Arrival Heights, Scott Base, Antarctica, we are able to analyze NWC phase measurements for the first time. Typically we expect near-linear phase responses to EEP flux variations rather than the more complex patterns of amplitude behavior as identified by *Clilverd et al.* [2008, Figure 5]. Figure 2 of the current paper shows three examples of the NWC nighttime phase variations at Casey (Figure 2, top) and Scott Base (Figure 2, bottom). The solid lines represent the nighttime data on 28 June 2009, 30 August 2009, and 28 May 2010, as labeled. The dotted lines represent the typical undisturbed behavior of the phase, taken from geomagnetically quiet days close to the event days. The undisturbed phase behavior shows a decrease in phase during sunset conditions on the propagation path (starting at ~09:00 UT in Figure 2)

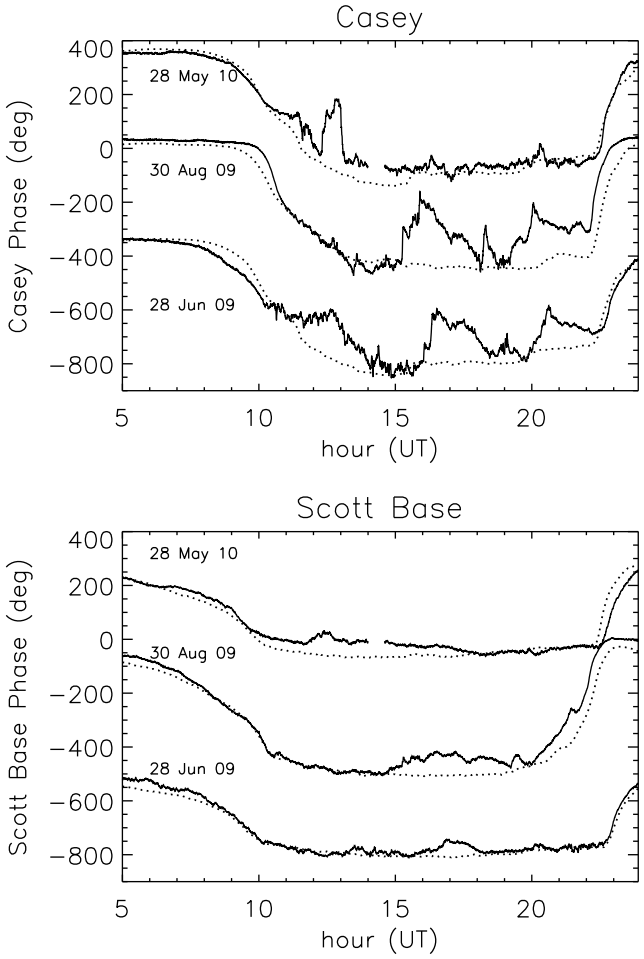

Figure 2. (top) The variation of nighttime phase from NWC to Casey on three typical event days in 2009–2010. The days have been offset to aid presentation. The normal quiet day behavior is shown by dotted lines. Electron precipitation events are observed as increases in phase, followed by a slow recovery to the quiet day levels. Phase decreases occur at sunset (~05:00–10:00 UT) and phase increases occur at sunrise (~21:00–24:00 UT). (bottom) Same as 2a, but for NWC received at Scott Base.

and an increase in phase during sunrise conditions (starting at ~22:00 UT in Figure 2). During the nighttime (~13:00–22:00 UT) the phase is relatively steady, and typically ~400° lower than during daytime. At 17:00 UT on 28 June 2009, 16:00 UT on 30 August 2009, and 12:00 UT on 28 May 2010, phase increases of ~200° are observed at Casey, with corresponding changes of ~40° at Scott Base. The enhancement of phase during these EEP events typically lasts 1–3 h, with the phase returning to near-undisturbed values by the end of the events. There are also NWC amplitude measurements available during these events, but highly variable winter-nighttime amplitude values make it difficult to accurately determine the undisturbed behavior, and as such we concentrate on phase measurements for this study.

[15] For one of the events shown, ~12:00 UT on 28 May 2010, the Southern Hemisphere footprint of the magnetic field line on which the THEMIS E spacecraft was located was close to the great circle paths between the NWC transmitter and the two receivers. Because of the extra detail that THEMIS can provide in terms of magnetic field measurements, and in situ observations of outer radiation belt electron populations [*Angelopoulos*, 2008], we concentrate on the 28 May 2010 event in detail for the remainder of this paper. Figure 3 shows the underlying geophysical conditions that were occurring around 28 May 2010. Panels in this figure show the variation of solar wind speed, D_{st}, K_p, and GOES >10 MeV proton fluence for 27–29 May 2010. A small but sudden increase in solar wind speed at ~02:00 UT on 28 May 2010 led to a small geomagnetic storm, with the main phase occurring on 29 May 2010, as evidenced by $D_{st} \approx -100$ and $K_p = 5$. During 28 May 2010, K_p increased gradually from very quiet levels to a slightly disturbed state (K_p = 0–3), and D_{st} became positive, with the solar wind remaining slightly elevated (~400 km s^{-1}). The lack of any change in the solar proton fluence panel indicates there was no solar proton event associated with this storm. These conditions are consistent with the initial phase of a geomagnetic storm.

[16] In Figure 4, we show the THEMIS E data during the 28 May 2010 event. The plot covers 10:00–14:00 UT. At this time THEMIS E was within 1° of the geomagnetic equator on the $L \sim 5.5$ field line and the Southern Hemisphere footprint of the magnetic field line passing through the satellite was in close proximity to the location of the Macquarie Island riometer (shown in Figure 1). This fortunate arrangement allows us to make detailed comparisons between the observations made by THEMIS E and the ground-based instrumentation. Figure 4 (top) shows the THEMIS SST electron flux variations for a number of energy ranges and indicates two periods of enhanced fluxes, one starting at 11:36 UT, peaking at 11:50 UT, and the second at 12:20 UT, peaking at 12:30 UT. Figure 4 (middle)

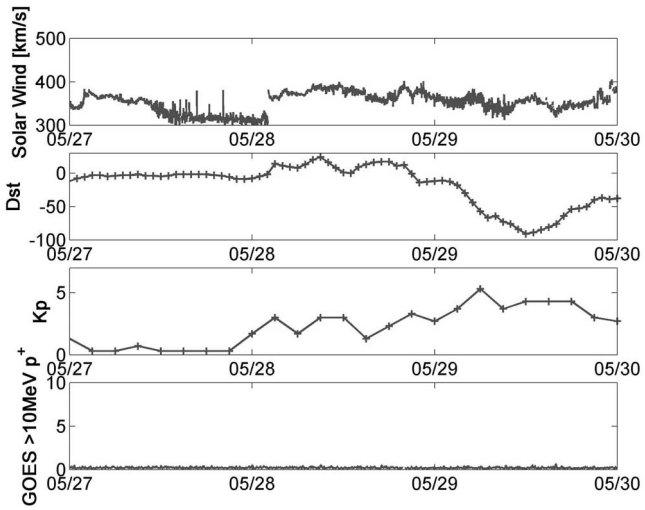

Figure 3. The background conditions for the 28 May 2010 precipitation event. The individual parts show the variations of solar wind speed, D_{st}, K_p, and GOES > 10 MeV proton fluence for 27–29 May 2010. The 28 May precipitation event occurs after a jump in solar wind speed, during the positive phase of a D_{st} disturbance, during low-moderate K_p levels, and with no enhancement of solar proton precipitation.

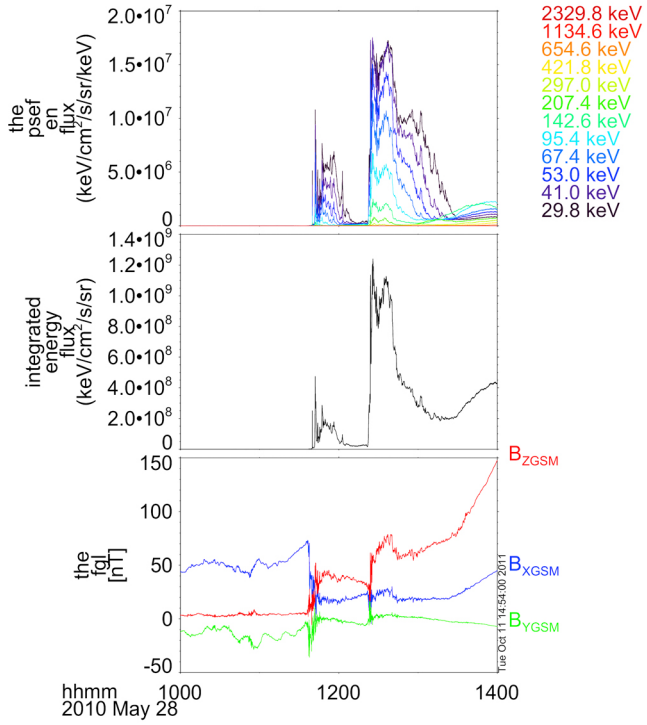

Figure 4. A summary plot of the THEMIS E SST data on 28 May 2010. (top) The variation in electron energy flux from 10:00 to 14:00 UT observed over a range of energy channels indicated by the colored labels on the right-hand side. (middle) The variation of the >30 keV integrated energy flux. (bottom) The variation of the magnetic field components in geocentric solar ecliptic (GSE) coordinates during the same period. Note the reversal of the x (blue line) and z (red line) components as a result of two substorm activations at ~11:36 UT and ~12:20 UT. The position of the satellite at 10:00 UT was $[x, y, z] = [-6.7, -7.2, 0.0]$, and at 14:00 UT was $[x, y, z] = [-1.2, -5.4, 0.2]$.

shows the same two periods of enhanced fluxes but as a function of >30 keV integrated energy flux. Figure 4 (bottom) shows the three-component magnetic field measurements in geocentric solar ecliptic (GSE) coordinates for the same period. The reversal of the x and z magnetic field components between 11:36 and 12:20 UT are indicative of two sequential substorm activations that show the increase in the Z component and a decrease in the X component of a dipolarization [*Lopez and Liu*, 1990] as the magnetic field changes from taillike to dipole-like. The largest fluxes observed by THEMIS E are seen after the second activation, from 12:20 to 13:30 UT, with elevated fluxes occurring in the energy range from 25 to 200 keV.

[17] The responses of the NWC signals received at Casey and Scott Base during 10:00–16:00 UT on 28 May 2010 are shown in Figure 5, top and middle, respectively. Vertical dash-dot lines indicate the timing shown by THEMIS observations in Figure 4, namely, the first substorm activation time of 11:36 UT and the second substorm activation time of 12:20 UT. The NWC-Casey phase variation shows two enhancements; the initial smaller event coincides with the first THEMIS substorm activation at ~11:36 UT but starts ~15 min earlier and shows phase changes of ~100°. The largest NWC phase change seen at Casey begins at ~12:20 UT and shows a double-peaked structure, initially at 12:30 UT with peak values of ~208°, eventually maximizing at 12:51 UT with phase change values of 265°. At Scott Base there is no obvious phase change associated with the first THEMIS substorm activation, but a gradual phase change starts at about 11:50 UT, with a small peak at 12:10 UT followed by a larger peak at about 12:30 UT. A comparison of the phase variations between Casey and Scott Base suggests that they follow a similar pattern, but with NWC-Scott Base leading the NWC-Casey substorm signature by about 20 min. However, the most likely explanation of these two data sets is that the NWC-Scott Base substorm signature is due to the first substorm, not to the second, and thus the peak phase effects appear delayed by ~34 min. This delay is difficult to explain, as at the substorm injection L shells ($L \sim 6$) of the NWC-Scott Base propagation path lie between NWC-Casey and the locations of Macquarie Island and the THEMIS magnetic field line footprint (see Figure 1). At 14:04 UT there was a NWC off-air period lasting for ~0.5 h. The timing of this in both the Casey and

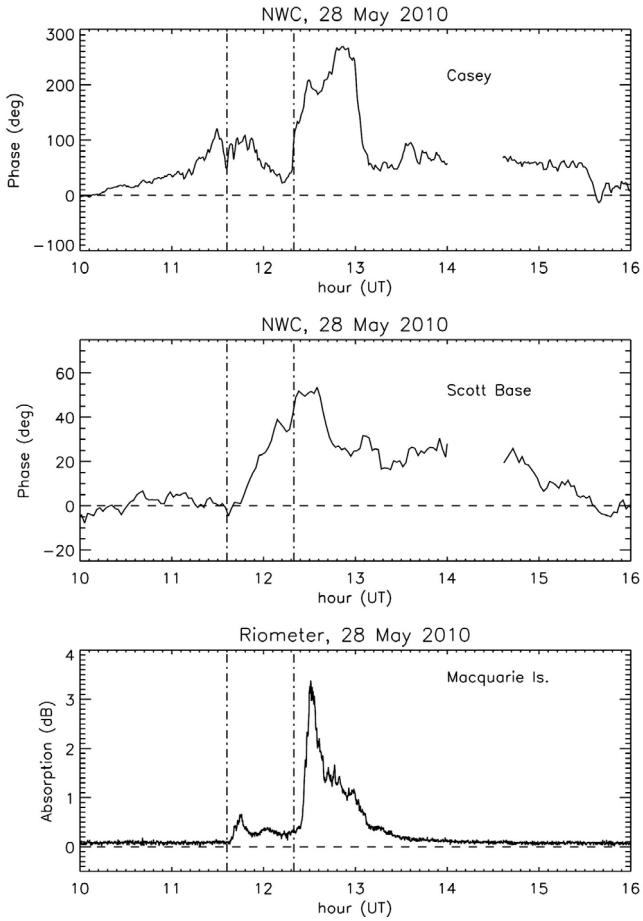

Figure 5. (top) The variation of NWC phase received at Casey for 10:00–16:00 UT on 28 May 2010. (middle) The variation of NWC phase received at Scott Base during the same period. (bottom) Macquarie Island riometer absorption during the same period. The times of the two substorm activations seen in THEMIS data are indicated by vertical dashed lines.

Scott Base NWC records indicates that the instrument clocks were accurate to <1 s during this period.

[18] The variation in absorption from the Macquarie Island riometer, situated at an L shell similar to that of the THEMIS observations, is plotted in the Figure 5 (bottom). As above, the timing of the THEMIS E substorm activation events shown in the Figure 4 (top) are indicated by vertical dot-dashed lines. The absorption shows a small increase following the start of the first THEMIS substorm activation and a larger increase at the time of the second activation, peaking at 12:30 UT with ~3.2 dB of absorption. Following the second peak, the absorption gradually recovers to near-zero levels at about the same time as the end of the second THEMIS substorm event. It is clear from this figure that the variation in riometer absorption is consistent with the variation in THEMIS E flux observations made at similar L shells and similar longitudes. Further, the timing of the peak absorption is coincident with the first of the two large peaks in the NWC phase change observed at Casey, i.e., at 12:30 UT.

[19] Thus, what we observe in this event are two substorm activations well described by THEMIS E measurements when the satellite is located on field lines close to Macquarie Island. The first substorm shows smaller flux enhancements than the second. The Macquarie Island riometer responds with a similar temporal variation compared with that of THEMIS, again with lower absorption enhancement during the first substorm compared with that of the second. The Casey NWC phase change shows some response at the time of the first and second substorms, with the second substorm peak phase effect larger than that of the first substorm. However, a further large change in the NWC-Casey phase occurs after both the THEMIS particle detectors and the Macquarie Island riometer have begun to recover back to nondisturbed levels during the second substorm, with NWC-Casey peaking about 25 min later. NWC-Scott Base phase changes show no immediate response to the first substorm activation, but thereafter show a double-peaked behavior that is similar to that of NWC-Casey but in advance of it by about 20 min. Clearly the NWC-Scott Base phase behavior is most likely to be associated with the first substorm, but the temporal evolution of the substorm precipitation region is unclear at this stage. The aim for this study is therefore to determine the relationship between the EEP fluxes observed by the ground-based instruments and those observed by the THEMIS E satellite, to answer why there are differences in response between the instruments during these substorms, and therefore why there are differences in the timing of the observed features.

4. Discussion

4.1. Modeling the EEP Flux

[20] In this subsection we model the effect that the substorm-driven EEP has on the riometer absorption signatures and compare the resulting estimate of precipitation fluxes with the observed radio wave propagation conditions among the Australian transmitter, NWC, and Casey. Previously *Clilverd et al.* [2008] used the LANL SOPA electron fluxes to investigate nondispersive injections of substorm-driven precipitation into the atmosphere. In that study EEP fluxes were used to model a substorm on 1 March 2006 that showed 3 dB of riometer absorption at Macquarie Island and ~−12 dB amplitude effect on an Australian transmitter, NTS, received at Casey. No phase observations were available at the time. Although not shown by *Clilverd et al.* [2008], amplitude measurements of NWC were made at Casey for that event and showed a decrease similar to that of NTS at Casey, i.e., ~−14 dB amplitude effect of the substorm-driven EEP. The substorm event reported here shows similar peak riometer absorption levels at similar MLTs (midnight) compared with the substorm on 1 March 2006 and with similar peak NWC amplitude changes of ~−9 dB. We note here that the identification of the quiet day curve for the NWC amplitude data at Casey, particularly that part during the nighttime in the winter months, is difficult and uncertain because of the high variability exhibited from day to day. However, the NWC quiet day phase variations are more consistent, and thus the identification of EEP effects on the NWC phase at Casey is a more reliable technique: hence the use of the NWC phase in the analysis undertaken in this paper.

[21] Given similar riometer substorm absorption levels, it seems reasonable to expect the LANL SOPA-based EEP spectrum used by *Clilverd et al.* [2008] to represent the EEP at the time of the peak riometer absorption conditions in this study. LANL SOPA data are currently unavailable to check this assumption. However, we are able to make use of the THEMIS SST electron channel measurements in order to estimate the EEP spectrum during this event. Figure 6 shows the electron flux from THEMIS E at the start of the second substorm (diamonds, labeled as 12:24 UT). Examination of the THEMIS SST data shows that the electron fluxes and spectral gradient remain essentially constant from 12:24 UT to 12:30 UT. Thus, although we often refer to the THEMIS data in terms of the 12:24 UT spectrum, it is also applicable to the spectrum when the riometer shows maximum absorption (12:30 UT). Figure 6 also shows the THEMIS electron flux at the peak of the NWC-Casey phase change (triangles, labeled as 12:51 UT). The solid line represents the electron spectrum determined from LANL during the peak of a similar substorm on 1 March 2006 [*Clilverd et al.*, 2008]. The dotted line represents a fit to the 12:51 UT electron spectra. The LANL spectra and the 12:24 UT THEMIS E spectra are very similar, while the 12:51 UT THEMIS E data show lower flux levels and a slightly harder spectrum. Figure 6 confirms the similarity in the substorm characteristics observed by LANL and by THEMIS and also confirms that there is little change in the electron spectrum as the substorm evolves. We note that the substorm electron precipitation spectrum reported by *Rosenberg et al.* [1972] was harder than that observed in this paper, although similar peak riometer absorption levels were recorded.

[22] Having determined the electron energy spectrum for the peak fluxes during each substorm event, we can now calculate the impact of electron precipitation on riometer absorption and radio wave propagation with different levels of flux. By calculating height-integrated differential absorption using a method described by *Thrane* [1973], we can estimate the EEP fluxes required to produce the observed substorm-driven riometer absorption for the Macquarie Island riometer at 12:30 UT on 28 May 2010. Figure 7 shows the change of riometer absorption and NWC phase received at Casey as a function of EEP integral flux >30 keV with units of cm^{-2} sr^{-1} s^{-1}, using the THEMIS-derived energy spectra from 12:24 UT. A vertical green line represents the

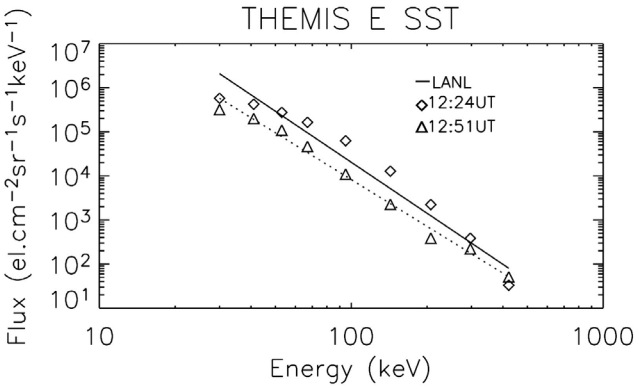

Figure 6. THEMIS E electron flux measurements at 12:24 UT (diamonds) and 12:51 UT (triangles) on 28 May 2010. The electron energy spectrum observed by LANL and presented by *Clilverd et al.* [2008] is shown by the solid line. The least squares fit to the 12:51 UT observations is given by the dotted line.

EEP flux levels that produce the observed effects on the riometer and NWC-Casey phase. The EEP-driven mesospheric ionization effects on VLF/LF wave propagation are modeled using the long-wave propagation code (LWPC) [*Ferguson and Snyder*, 1990]. The LWPC models VLF signal propagation from any point on Earth to any other point. Given electron density profile parameters for the upper boundary conditions, the LWPC calculates the expected amplitude and phase of the VLF signal at the reception point. As *Clilverd et al.* [2008] did, we use a simple ionospheric model to describe the balance of electron number density N_e in the lower ionosphere, based on that given by *Rodger et al.* [1998] and further described by *Rodger et al.* [2007a]. The electron number density profiles determined using the simple ionospheric electron model for varying precipitation flux magnitudes (30 keV–2.5 MeV) are used as input to the LWPC subionospheric propagation model. Consistent with the work of *Berkey et al.* [1974], the EEP-affected profiles are applied on only a portion of the transmitter-receiver great circle path between $L = 5.2$ and $L = 8.9$, thus modeling the effect of precipitation on the NWC phase received at Casey. The effects of the EEP are compared with undisturbed LWPC model phase values for the path using the nighttime model ionosphere of *Thomson et al.* [2007]. A more detailed description of this technique can be found in the work by *Clilverd et al.* [2008].

[23] Throughout this study we assume that the EEP fluxes and spectra are the same over the whole L shell range affected by the EEP. The substorm L shell range is based on the average EEP range presented by *Berkey et al.* [1974], with fine tuning provided by the intercomparison between riometer absorption observations and the NWC-Casey phase change. Future challenges for this work will be to include L shell variations in spectra [e.g., *Liu et al.*, 2009b] and L shell variations in flux.

[24] The results shown in Figure 7 indicate the integral >30 keV flux levels required to generate the observed maximum effects on riometer and radio wave data at 12:30 UT during the second substorm. Both riometer absorption and the NWC phase show well-ordered responses to increased EEP fluxes. This is in contrast to radio wave amplitude responses in which an observed amplitude value could have more than one EEP flux solution [see *Clilverd et al.*, 2008, Figure 5, and *Rodger et al.*, 2007c, Figure 7]. Thus, the phase analysis performed here allows a clearer identification of the incident EEP flux during the substorm, with less likelihood of a nonunique solution. Figure 7 also confirms that the EEP spectrum used is able to produce both the observed riometer absorption levels and the observed NWC-Casey phase change using the same EEP flux value, assuming a realistic L shell range over which the EEP was applied to the NWC-Casey propagation path (about $5 < L < 9$). The modeling indicates that the same EEP also reproduces the peak NWC-Casey amplitude change. The EEP flux level identified by the vertical green line (>30 keV 5.6×10^7 el cm^{-2} sr^{-1} s^{-1}) is 80% of the LANL SOPA peak substorm integrated flux of 1 March 2006 reported by *Clilverd et al.* [2008].

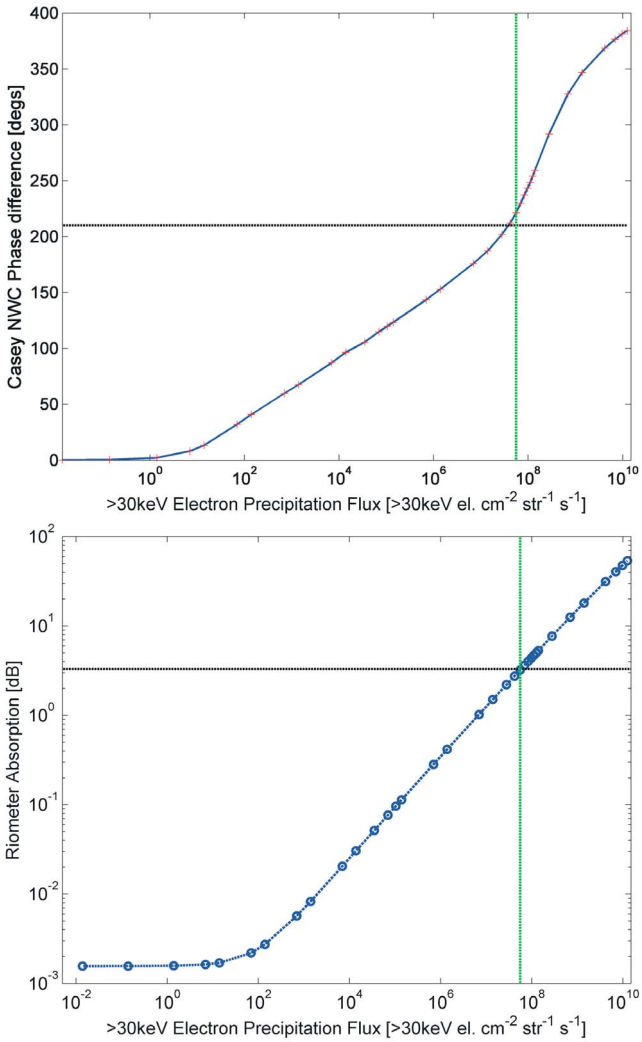

Figure 7. (top) The calculated NWC phase change as a function of electron precipitation flux >30 keV at Casey. (bottom) The equivalent riometer absorption level at Macquarie Island. The green vertical line indicates the flux levels required to reproduce the NWC-Casey phase and riometer absorption values at the peak of the second substorm (values indicated by horizontal gray lines).

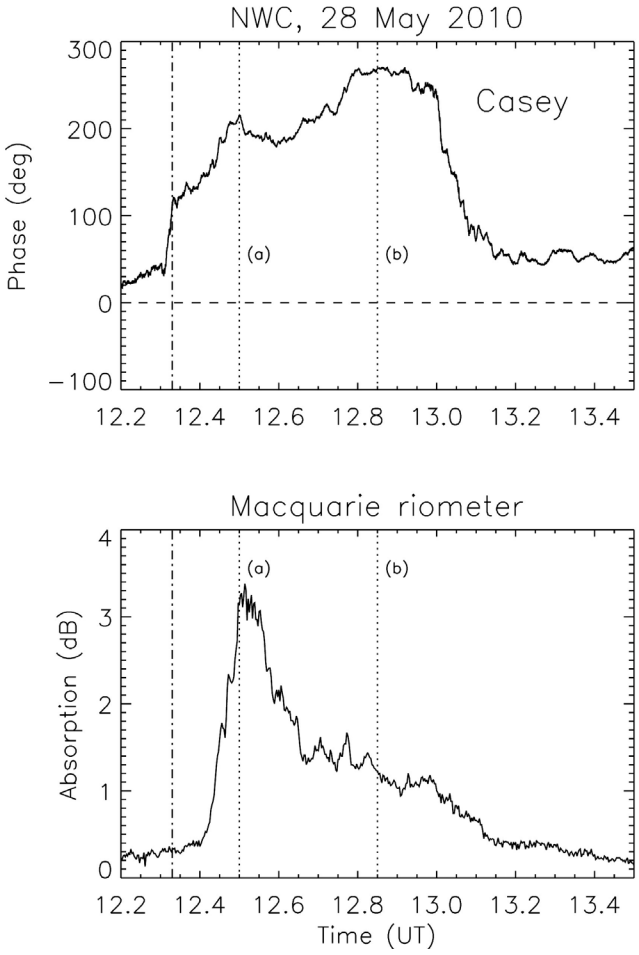

Figure 8. (top) NWC phase change at Casey during second substorm event. (bottom) Macquarie Island riometer absorption. The vertical dot-dashed line indicates the start of the substorm event as determined by THEMIS E magnetometer dipolarization timing. The vertical dotted lines labeled (a) and (b) indicate the timing of the peak riometer absorption and the peak phase change, respectively.

[25] The first substorm produced 0.6 dB of riometer absorption and 100° of phase change on NWC-Casey. Using the results shown in Figure 7, we can determine that the EEP flux level of >30 keV 2×10^6 el cm^{-2} sr^{-1} s^{-1} (an integrated energy flux of 1.4 ergs cm^{-2} sr^{-1} s^{-1}) is required to reproduce the riometer absorption. However, assuming a precipitation region that covers $5 < L < 9$, as shown in Figure 7, we would expect 150° of phase change on the NWC-Casey propagation path. The smaller phase change observed therefore suggests that the injection region of the first substorm precipitation region is either latitudinally smaller than the second substorm or the NWC-Casey response seen at the time of the substorm is not associated with substorm EEPs.

4.2. Time Evolution of the EEP

[26] Here we investigate the time evolution of the second activation event in which the riometer absorption peaks at a different time to the peak Casey phase change. Figure 8 shows the second substorm event in detail for NWC-Casey phase change (Figure 8, top) and for the Macquarie Island riometer absorption (Figure 8, bottom). The vertical dot-dashed line in each panel indicates the time of the onset of the substorm, while two vertical dotted lines indicate the timing of the peak in riometer absorption at 12:30 UT (line (a)) and the timing of the peak in the Casey phase change at 12:51 UT (line (b)). In section 4.1 we successfully modeled the former; that is, the riometer absorption and phase response observed at Casey at the same time, i.e., time of line (a). However, the increase in NWC-Casey phase change at line (b) relative to that of line (a) suggests that the NWC-Casey propagation path is experiencing more ionization at this time, although, conversely, the reduction in the riometer absorption suggests less ionization. These changes are consistent either with a change in EEP spectral gradients to higher energies (away from the energies that riometers are sensitive to, i.e., ~30 keV electrons) or an increase in the proportion of the NWC-Casey propagation path that is experiencing EEP. In Figure 6 we showed that the THEMIS electron spectrum changed only a small amount as the substorm evolved from (a) to (b), and calculations similar to those undertaken in section 4.1 suggest that the small change in spectrum observed could not explain the relative changes in phase or absorption. Thus we conclude that the spectrum remains relatively unchanged and that the proportion of the NWC-Casey propagation path experiencing EEP has increased.

[27] *Berkey et al.* [1974] observed an expansion poleward and equatorward of the precipitation initiation region shortly after the substorm began. Using an extended precipitation region, the THEMIS spectrum taken at 12:51 UT, we were able to reproduce both the NWC phase change and the riometer absorption values at line (b) in Figure 8. The expanded precipitation region required is $4.2 < L < 12.6$ and the reduced fluxes of >30 keV were 7.8×10^6 el cm^{-2} sr^{-1} s^{-1} (an integrated energy flux of 0.2 ergs cm^{-2} sr^{-1} s^{-1}). This is consistent with the observations of *Berkey et al.* [1974], which gave $4 < L < 12$. We note here that the riometer absorption data allow us to determine the change in flux in this case, as Macquarie Island remains under the region of precipitation at all times during the substorm.

4.3. Substorm EEP Eastward of the Injection Region

[28] So far, we have considered the substorm-driven EEP affects on the Macquarie Island riometer and the NWC transmitter signal received at Casey and Scott Base. From Figure 1 it is apparent that the NWC signals cross under the $L = 6$ contour west of Macquarie Island. However, the region of electron precipitation is expected to expand eastward at the approximate drift velocity of electrons with energies of 50–300 keV [*Berkey et al.*, 1974]. Figure 1 indicates that the NPM, Hawaii, signals have paths that cut the $L = 6$ contour close to Macquarie Island (154° longitude, NPM to Casey) and east of Macquarie Island (186° longitude, NPM to Scott Base), so we might expect to see delayed substorm effects, particularly on the easternmost path. We plot the NPM phase change from Scott Base and Casey in Figure 9. The format is similar to that of previous plots, with the vertical dashed lines representing the two substorm activation times at 11:36 UT and 12:20 UT. It is clear that the peak phase changes for the two substorms occur at different times at the two receiver sites, with NPM-Scott Base being delayed by 20 min for the first substorm and 42 min for the second substorm. The NPM-Casey substorm

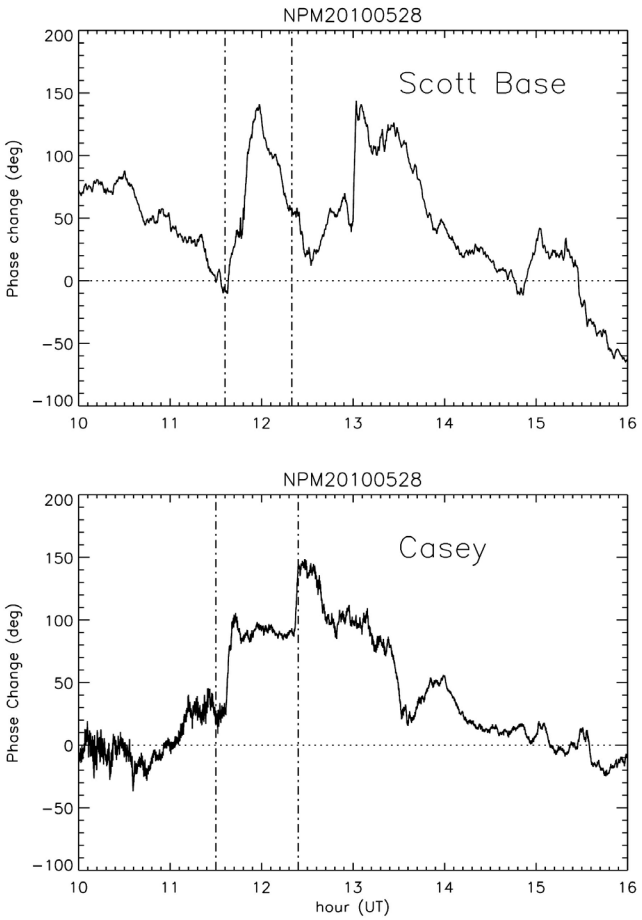

Figure 9. The NPM-Scott Base and NPM-Casey phase changes at 10:00–16:00 UT, 28 May 2010. Vertical lines represent the activation times of the two substorms.

signatures show a delay of ~5 min for the first substorm and no delay for the second substorm. Hence, taking into account the eastward expansion of the EEP and the timing of substorm signatures in all the data sets, we estimate that the initial EEP injection spans the region 130°E–150°E for the first substorm and 110°E–150°E for the second substorm.

[29] Using expressions from the work by *Walt* [1994], we find that the azimuthal drift period around the Earth for electrons at $L = 6$ with a pitch angle of 90°, i.e., equatorially trapped, of 50 keV electrons is 154 min. For 300 keV electrons it is 30 min. The NPM-Scott Base path cuts the $L = 6$ contour at 186°E. Thus 50 keV electrons would take 15–34 min to travel to this longitude from the extended injection region, which is consistent with the 20 and 42 min delays observed for the first and second substorms, respectively. Further, higher-energy electrons such as 300 keV would drift from the injection region to 186°E in 2.5–7 min, so we would expect the phase response of NPM at Scott Base to start to respond soon after the substorm activation and then increase gradually as high fluxes of lower-energy electrons arrived. This is what is seen in the experimental observations. The lowest-energy electrons that are likely to influence the VLF transmitter propagation at night are ~50 keV. Electrons with energies <50 keV will produce excess ionization at altitudes above the bottom of the *D* region [*Turunen et al.*, 2009], and hence the VLF signals propagating at grazing incidence will be insensitive to the excess ionization. Consequently, the delay of the peak of the phase change will be due to the timing of the highest fluxes of >50 keV electrons, which will be when the ~50 keV electron precipitation has had time to drift around to 186°E longitude.

4.4. The Unexplained NWC-Scott Base Phase Changes

[30] Figure 5, top, shows the NWC-Casey phase change during the substorm period. Figure 5, middle, shows the NWC-Scott Base phase change, and although there is a strong similarity in the phase change patterns, there appears to be a time shift between the two by 20 min with NWC-Scott Base leading NWC-Casey. This suggests that the phase change on the NWC-Scott Base propagation path is driven in a way similar to that of NWC-Casey, but 20 min earlier. This

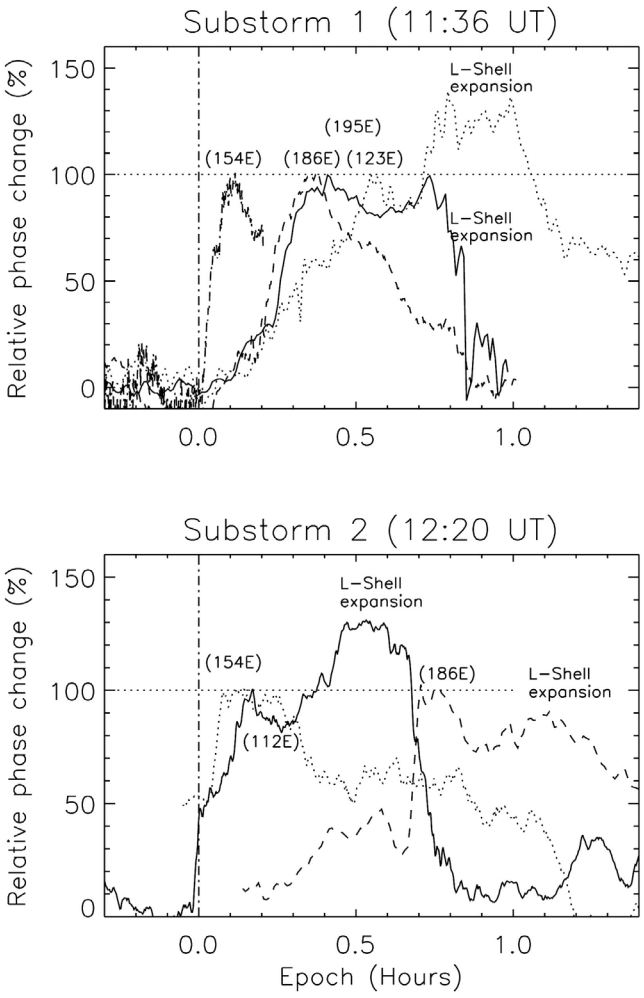

Figure 10. A summary of the phase changes observed during (top) substorm 1 and (bottom) substorm 2. The phase change is expressed as a percentage, with 100% defined as the maximum phase change caused by the substorm injections. The longitude of each propagation path where it cuts the $L = 6$ contour (as shown in Figure 1) is indicated, e.g., 112°E (NWC-Casey), 123°E (NWC-Scott Base), 154°E (NPM-Casey), 186°E (NPM-Scott Base), and 195°E (NLK-Scott Base). The periods of expanding the *L* shell extent of the substorm-induced EEP are indicated.

result can be explained only if the NWC-Scott Base phase effects are due to the EEP from the first substorm (and hence correspond to a delay of ~34 min) while the NWC-Casey phase effect must be due to the second substorm. We note here that the instrument timings at Casey and Scott Base are accurate to <1 s and that there is no offset between them.

[31] We separate the peak phase changes associated with substorm 1 and substorm 2 and show them in two parts in Figure 10. The plot shows the phase changes observed during substorm 1 (Figure 10, top) and substorm 2 (Figure 10, bottom) expressed as a percentage, where 100% is defined as the maximum phase change caused by the initial substorm injections on each individual propagation path and not the phase change associated with the latitudinal expansion that follows. The longitude of each propagation path where it cuts the $L = 6$ contour (indicated in Figure 1) is provided as a label, e.g., 112°E (NWC-Casey), 123°E (NWC-Scott Base), 154°E (NPM-Casey), 186°E (NPM-Scott Base), and 200°E (NLK-Scott Base). Substorm 1 shows an increasing delay of the peak phase effect with eastward longitude, particularly shown by NPM-Scott Base and NLK-Scott Base. Typically we observe drifts of 35°–40° eastward in ~20 min. This corresponds to a drift period of 180 min, which is equivalent to the drift period of ~40 keV electrons at $L = 6$. We note that all longitudes show an almost immediate phase increase response to the substorm injection, exhibiting delays of <3 min for ~40° of longitude drift and therefore evidence of the injection of electron energies of ~1 MeV.

[32] In substorm 2 we find that the paths with $L = 6$ crossing points at longitudes of 112°E (NWC-Casey) and 154°E (NPM-Casey) react at about the same time, suggesting an injection region somewhere in between the two longitudes, while 186°E (NPM-Scott Base) shows a peak phase effect with a delay of 40 min that suggests a drift period of ~400 min and therefore electron energies of ~20 keV. This suggests that electron precipitation is occurring, involving lower energies in the second substorm compared with those of the first; hence the longer drift delays observed.

[33] In the first substorm, Figure 10 shows that the westernmost path (123°E, NPM-Casey) reaches its peak phase change later than all of the other paths plotted. This is consistent with the results of *Berkey et al.* [1974], who showed that despite the general picture of eastward electron drift dominating, there can be some westward expansion of the precipitation region that is usually slower than the eastward drift rate and that may be associated with the westward traveling surge in the visual aurora.

[34] Given the understanding of the generally eastward progression in the peak phase changes in Figure 10, we can see that the first substorm initially does not show the latitudinal expansion in the precipitation region to $4 < L < 12$, as discussed earlier in the paper, i.e., no obvious L shell expansion identified on the 154°E and 186°E longitudes. The easternmost path, NLK-Scott Base at ~200°E, shows evidence of this happening, as does the westernmost path NWC-Scott Base (123°E), significantly later on. This indicates that, as far as the VLF observations are concerned, the L shell expansion occurs ~40 min after the initial injection, both to the east and to the west of the injection region. Further modeling of the time variation of the EEP fluxes and L shell coverage will be undertaken in a future study.

[35] For the second substorm, the latitudinal expansion happens on NWC-Casey at ~112°E, with the shortest delay time we observed of 30 min, and on NPM-Scott Base at ~186°E, much later on at ~70 min. As in the first substorm, the path in between (154°E) shows a much weaker L shell expansion signature. This suggests that the second substorm is more dynamic in its expansion westward than the first. Thus we conclude that although both substorms occurred at similar local times, with EEP injections into the same geographical region, there are significant differences in behavior between the two. To the east of the initial injection region, the timing of the latitudinal expansion appears to be a function of the longitudinal expansion rate, and there is nearly a factor of 2 difference between the two substorms. To the west, the relationship between latitudinal and longitudinal expansion appears reversed compared with that of the east.

5. Summary

[36] In this study we examine energetic electron precipitation characteristics from two substorm precipitation events on 28 May 2010. The substorms occurred near MLT midnight in the New Zealand/Australia sector, with signatures observed from 11:36 UT until ~13:30 UT. We present AARDDVARK ground-based radio wave phase observations from NWC, Australia, NPM, Hawaii, and NLK, Seattle, received at Casey, Antarctica (66.3°S, 110.5°E, $L > 999$) and Scott Base, Antarctica (77.8°S, 166.8°E, $L > 32$). We also include the Macquarie Island riometer absorption data (54.5°S, 158.9°E, $L = 5.4$), and THEMIS E Solid State Telescope (SST) observations. All three instruments observed substorm signatures during the substorm events, consistent with their colocation in the longitudes of Australia. The THEMIS E magnetic field components showed clear signatures of dipolarization at the times of both substorm activations.

[37] It was possible to accurately reproduce the peak observed riometer absorption at Macquarie Island (3.2 dB, $L = 5.4$) and the associated NWC radio wave phase change observed at Casey, Antarctica (208°). We used an electron precipitation spectrum taken from THEMIS E electron flux measurements, which was consistent with the LANL-97A energetic electron flux measurements from a similar substorm studied by *Clilverd et al.* [2008]. Our calculations were based on modeling the impact of energetic electron precipitation in a region covering $5 < L < 9$. This is consistent with the concept that the electron precipitation injection region is restricted to near-geosynchronous orbit L shells. The flux levels required of >30 keV 5.6×10^7 el cm^{-2} sr^{-1} s^{-1} (an integrated energy flux of 1.4 ergs cm^{-2} sr^{-1} s^{-1}) were 80% of the peak fluxes observed in a similar substorm by LANL-97A in 2007 by *Clilverd et al.* [2008].

[38] The largest phase change seen at Casey showed a double-peaked structure, initially at 12:30 UT with peak values of ~208°, eventually maximizing at 12:51 UT with phase change values of 265°. Using an extended precipitation region after the initial injection, consistent with the work of *Berkey et al.* [1974], the THEMIS electron spectrum taken at 12:51 UT, we were able to reproduce both the NWC phase change and associated riometer absorption values of 1.2 dB. The extended precipitation region was $4.2 < L < 12.6$ and the >30 keV flux was 7.8×10^6 el cm^{-2} sr^{-1} s^{-1} (an integrated energy flux of 0.2 ergs cm^{-2} sr^{-1} s^{-1}). Thus, we

show that by using a single riometer site in combination with a single AARDDVARK radio wave receiver site, we are in principle able to describe the evolution of the substorm precipitation flux and the latitudinal expansion of the substorm region.

[39] In this study of a pair of substorm events, we conclude that although both substorms occurred at similar local times, with EEP injections into approximately the same geographical region, the first substorm involved less EEP flux, but the precipitation region drifted eastward more quickly than the second, larger event. This study has shown that it is possible to successfully combine AARDDVARK radio wave observations, THEMIS satellite measurements, and riometer absorption data in order to investigate the characteristics of substorm-induced energetic electron precipitation in detail.

[40] **Acknowledgments.** The authors would like to acknowledge the support of the Australian Antarctic Division project ASAC 1324 for the Casey data and, in particular, the assistance of Ian Phillips. We would also like to acknowledge the use of the AAD data system for the provision of the Macquarie Island Riometer data (http://www.ips.gov.au/World_Data_Centre/1/8). The Scott Base experiment is supported by Antarctica New Zealand, event K060. We acknowledge NASA contract NAS5–02099 and V. Angelopoulos for the use of data from the THEMIS mission. Specifically, we thank D. Larson and R. P. Lin for use of the SST data. I.J.R. is funded by the Canadian Space Agency. The research leading to these results has received funding from the European Union Seventh Framework Programme (FP7/2007–2013) under grant agreement 263218.

[41] Masaki Fujimoto thanks the reviewers for their assistance in evaluating the paper.

References

Akasofu, S.-I. (1964), The development of the auroral substorm, *Planet. Space Sci.*, *12*, 273–282, doi:10.1016/0032-0633(64)90151-5.

Angelopoulos, V. (2008), The THEMIS mission, *Space Sci. Rev.*, *141*, 5–34, doi:10.1007/s11214-008-9336-1.

Axford, W. (1999), Reconnection, substorms and solar flares, *Phys. Chem. Earth Part C*, *24*, 147–151, doi:10.1016/S1464-1917(98)00022-1.

Bailey, D. K. (1968), Some quantitative aspects of electron precipitation in and near the auroral zone, *Rev. Geophys.*, *6*, 289–346, doi:10.1029/RG006i003p00289.

Baker, D. N., W. Aiello, J. R. Asbridge, R. D. Belian, P. R. Higbie, R. W. Klebesadel, J. G. Laros and E. R. Tech (1985), Los Alamos energetic particle sensor systems at geostationary orbit," *AIAA Pap. 85–0243*.

Barr, R., D. L. Jones, and C. J. Rodger (2000), ELF and VLF radio waves, *J. Atmos. Sol. Terr. Phys.*, *62*, 1689–1718, doi:10.1016/S1364-6826(00)00121-8.

Berkey, F. T., V. M. Driatskiy, K. Henriksen, B. Hultqvist, D. H. Jelly, T. I. Shchuka, A. Theander, and J. Yliniemi (1974), A synoptic investigation of particle precipitation dynamics for 60 substorms in IQSY (1964–1965) and IASY (1969), *Planet. Space Sci.*, *22*, 255–307, doi:10.1016/0032-0633(74)90028-2.

Brasseur, G., and S. Solomon (2005), *Aeronomy of the Middle Atmosphere*, 3rd ed., D. Reidel, Dordrecht, Netherlands.

Clilverd, M. A., et al. (2008), Energetic electron precipitation during sub-storm injection events: High-latitude fluxes and an unexpected mid-latitude signature, *J. Geophys. Res.*, *113*, A10311, doi:10.1029/2008JA013220.

Clilverd, M. A., et al. (2009), Remote sensing space weather events: The AARDDVARK network, *Space Weather*, *7*, S04001, doi:10.1029/2008SW000412.

Clilverd, M. A., C. J. Rodger, R. J. Gamble, T. Ulich, T. Raita, A. Seppälä, J. C. Green, N. R. Thomson, J.-A. Sauvaud, and M. Parrot (2010), Ground-based estimates of outer radiation belt energetic electron precipitation fluxes into the atmosphere, *J. Geophys. Res.*, *115*, A12304, doi:10.1029/2010JA015638.

Ferguson, J. A., and F. P. Snyder (1990), Computer programs for assessment of long wavelength radio communications, *Tech. Doc. 1773*, Natl. Ocean Syst. Cent., San Diego, California.

Jelly, D., and N. Brice (1967), Changes in the Van Allen radiation associated with polar substorms, *J. Geophys. Res.*, *72*(23), 5919–5931, doi:10.1029/JZ072i023p05919.

Kavanagh, A. J., G. Lu, E. F. Donovan, G. D. Reeves, F. Honary, J. Manninen, and T. J. Immel (2007), Energetic electron precipitation during sawtooth injections, *Ann. Geophys.*, *25*, 1199–1214, doi:10.5194/angeo-25-1199-2007.

Little, C. G., and H. Leinbach (1959), The riometer: A device for the continuous measurements of ionospheric absorption, *Proc. IRE*, *37*, 315–320.

Liu, J., et al. (2009a), THEMIS observation of a substorm event on 04:35, 22 February 2008, *Ann. Geophys.*, *27*, 1831–1841, doi:10.5194/angeo-27-1831-2009.

Liu, W. L., X. Li, T. Sarris, C. Cully, R. Ergun, V. Angelopoulos, D. Larson, A. Keiling, K. H. Glassmeier, and H. U. Auster (2009b), Observations and modeling of the injection observed by THEMIS and LANL satellites during the 23 March 2007 substorm event, *J. Geophys. Res.*, *114*, A00C18, doi:10.1029/2008JA013498.

Lopez, R. E., and A. T. Y. Liu (1990), A multisatellite case study of the expansion of a substorm current wedge in the near-earth magnetotail, *J. Geophys. Res.*, *95*(A6), 8009–8017, doi:10.1029/JA095iA06p08009.

Lorentzen, K. R., J. B. Blake, U. S. Inan, and J. Bortnik (2001), Observations of relativistic electron microbursts in association with VLF chorus, *J. Geophys. Res.*, *106*, 6017–6027, doi:10.1029/2000JA003018.

Millan, R. M., R. P. Lin, D. M. Smith, K. R. Lorentzen, and M. P. McCarthy (2002), X-ray observations of MeV electron precipitation with a balloon-borne germanium spectrometer, *Geophys. Res. Lett.*, *29*(24), 2194, doi:10.1029/2002GL015922.

Nagai, T., M. Fujimoto, Y. Saito, S. Machida, T. Terasawa, R. Nakamura, T. Yamamoto, T. Mukai, A. Nishida, and S. Kokubun (1998), Structure and dynamics of magnetic reconnection for substorm onsets with Geotail observations, *J. Geophys. Res.*, *103*, 4419–4440, doi:10.1029/97JA02190.

Randall, C. E., et al. (2005), Stratospheric effects of energetic particle precipitation in 2003–2004, *Geophys. Res. Lett.*, *32*, L05802, doi:10.1029/2004GL022003.

Reeves, G., A. Chan, and C. J. Rodger (2009), New directions for radiation belt research, *Space Weather*, *7*(7), S07004, doi:10.1029/2008SW000436.

Rodger, C. J., O. A. Molchanov, and N. R. Thomson (1998), Relaxation of transient ionization in the lower ionosphere, *J. Geophys. Res.*, *103*(A4), 6969–6975, doi:10.1029/98JA00016.

Rodger, C. J., M. A. Clilverd, N. R. Thomson, R. J. Gamble, A. Seppälä, E. Turunen, N. P. Meredith, M. Parrot, J. A. Sauvaud, and J.-J. Berthelier (2007a), Radiation belt electron precipitation into the atmosphere: Recovery from a geomagnetic storm, *J. Geophys. Res.*, *112*, A11307, doi:10.1029/2007JA012383.

Rodger, C. J., M. A. Clilverd, D. Nunn, P. T. Verronen, J. Bortnik, and E. Turunen (2007b), Storm time, short-lived bursts of relativistic electron precipitation detected by subionospheric radio wave propagation, *J. Geophys. Res.*, *112*, A07301, doi:10.1029/2007JA012347.

Rodger, C. J., M. A. Clilverd, N. R. Thomson, R. J. Gamble, A. Seppälä, E. Turunen, N. P. Meredith, M. Parrot, J. A. Sauvaud, and J.-J. Berthelier (2007c), Radiation belt electron precipitation into the atmosphere: Recovery from a geomagnetic storm, *J. Geophys. Res.*, *112*, A11307, doi:10.1029/2007JA012383.

Rodger, C. J., T. Raita, M. A. Clilverd, A. Seppälä, S. Dietrich, N. R. Thomson, and T. Ulich (2008), Observations of relativistic electron precipitation from the radiation belts driven by EMIC waves, *Geophys. Res. Lett.*, *35*, L16106, doi:10.1029/2008GL034804.

Rodger, C. J., M. A. Clilverd, J. Green, and M.-M. Lam (2010a), Use of POES SEM-2 observations to examine radiation belt dynamics and energetic electron precipitation in to the atmosphere, *J. Geophys. Res.*, *115*, A04202, doi: 10.1029/2008JA014023.

Rodger, C. J., M. A. Clilverd, A. Seppälä, N. R. Thomson, R. J. Gamble, M. Parrot, J.-A. Sauvaud, and T. Ulich (2010b), Radiation belt electron precipitation due to geomagnetic storms: Significance to middle atmosphere ozone chemistry, *J. Geophys. Res.*, *115*, A11320, doi:10.1029/2010JA015599.

Rosenberg, T. J., L. J. Lanzerotti, D. K. Bailey, and J. D. Pierson (1972), Energy spectra in relativistic electron precipitation events, *J. Atmos. Terr. Phys.*, *34*, 1977–1990, doi:10.1016/0021-9169(72)90179-1.

Sandholt, P. E., C. J. Farrugia, M. Lester, S. Cowley, S. Milan, W. F. Denig, B. Lybekk, E. Trondsen, and V. Vorobjev (2002), Multistage substorm expansion: Auroral dynamics in relation to plasma sheet particle injection, precipitation, and plasma convection, *J. Geophys. Res.*, *107*(A11), 1342, doi:10.1029/2001JA900116.

Seppälä, A., M. A. Clilverd, and C. J. Rodger (2007), NOx enhancements in the middle atmosphere during 2003–2004 polar winter: Relative significance of solar proton events and the aurora as a source, *J. Geophys. Res.*, *112*, D23303, doi:10.1029/2006JD008326.

Seppälä, A., C. E. Randall, M. A. Clilverd, E. Rozanov, and C. J. Rodger (2009), Geomagnetic activity and polar surface level air temperature variability, *J. Geophys. Res.*, *114*, A10312, doi:10.1029/2008JA014029.

Spanswick, E., E. Donovan, R. Friedel, and A. Korth (2007), Ground based identification of dispersionless electron injections, *Geophys. Res. Lett.*, *34*, L03101, doi:10.1029/2006GL028329.

Spanswick, E., E. Donovan, W. Liu, J. Liang, J. B. Blake, G. Reeves, R. Friedel, B. Jackel, C. Cully, and A. Weatherwax (2009), Global observations of substorm injection region evolution: 27 August 2001, *Ann. Geophys.*, *27*, 2019–2025, doi:10.5194/angeo-27-2019-2009.

Thomson, N. R., M. A. Clilverd, and W. M. McRae (2007), Nighttime ionospheric *D* region parameters from VLF phase and amplitude, *J. Geophys. Res.*, *112*, A07304, doi:10.1029/2007JA012271.

Thorne, R. M., and T. R. Larsen (1976), An investigation of relativistic electron precipitation events and their association with magnetic substorm activity, *J. Geophys. Res.*, *81*(31), 5501–5506, doi:10.1029/JA081i031p05501.

Thrane, E. V. (1973), Radiowave propagation, in *Cosmical Geophysics*, edited by A. Egeland et al., pp. 267–281, Universitetsforlaget, Oslo, Norway.

Turunen, E., P. T. Verronen, A. Seppälä, C. J. Rodger, M. A. Clilverd, J. Tamminen, C. F. Enell, and T. Ulich (2009), Impact of different precipitation energies on NO_x generation during geomagnetic storms, *J. Atmos. Sol. Terr. Phys.*, *71*, 1176–1189, doi:10.1016/j.jastp.2008.07.005.

Verronen, P. T., C. J. Rodger, M. A. Clilverd, and S. Wang (2011), First evidence of mesospheric hydroxyl response to electron precipitation from the radiation belts, *J. Geophys. Res.*, *116*, D07307, doi:10.1029/2010JD014965.

Walt, M. (1994), *Introduction to Geomagnetically Trapped Radiation, Cambridge Atmospheric and Space Series*, 49 pp., Cambridge Univ. Press, Cambridge, UK, doi:10.1017/CBO9780511524981.

J. B. Brundell, C. J. Rodger, and N. R. Thomson, Department of Physics, University of Otago, PO Box 56, Dunedin, 9054, New Zealand.

M. A. Clilverd and N. Cobbett, British Antarctic Survey, High Cross, Madingley Rd., Cambridge CB3 0ET, UK.

F. W. Menk, School of Mathematical and Physical Sciences, University of Newcastle, Mathematics Building V201B, Callaghan, New South Wales, 2308, Australia.

I. J. Rae, Department of Physics, University of Alberta, Edmonton, Canada.

P. T. Verronen, Finnish Meteorological Institute, PO Box, 503, 00101 Helsinki, Finland.